

Crystal structure of calcium-ferrite type NaAlSiO₄ up to 45 GPa

FEI QIN^{1,2,*}, YE WU^{3,†}, SHENGCHAO XUE¹, DONGZHOU ZHANG^{4,‡}, XIANG WU⁵, AND STEVEN D. JACOBSEN^{2,§}

¹School of Earth Sciences and Resources, China University of Geosciences (Beijing), Beijing, China

²Department of Earth and Planetary Sciences, Northwestern University, Evanston, Illinois, 60208, U.S.A.

³School of Science, Wuhan University of Technology, Wuhan, China

⁴School of Ocean and Earth Science and Technology, Hawai'i Institute of Geophysics and Planetology, University of Hawaii at Manoa, Honolulu, Hawaii 96822, U.S.A.

⁵State Key Laboratory of Geological Processes and Mineral Resources, China University of Geosciences, Wuhan, China

ABSTRACT

Alkali-rich aluminous high-pressure phases including calcium-ferrite (CF) type NaAlSiO₄ are thought to constitute ~20% by volume of subducted mid-ocean ridge basalt (MORB) under lower mantle conditions. As a potentially significant host for incompatible elements in the deep mantle, knowledge of the crystal structure and physical properties of CF-type phases is therefore important to understanding the crystal chemistry of alkali storage and recycling in the Earth's mantle. We determined the evolution of the crystal structure of pure CF-NaAlSiO₄ and Fe-bearing CF-NaAlSiO₄ at pressures up to ~45 GPa using synchrotron-based, single-crystal X-ray diffraction. Using the high-pressure lattice parameters, we also determined a third-order Birch-Murnaghan equation of state, with $V_0 = 241.6(1) \text{ \AA}^3$, $K_{70} = 220(4) \text{ GPa}$, and $K'_{70} = 2.6(3)$ for Fe-free CF, and $V_0 = 244.2(2) \text{ \AA}^3$, $K_{70} = 211(6) \text{ GPa}$, and $K'_{70} = 2.6(3)$ for Fe-bearing CF. The addition of Fe into CF-NaAlSiO₄ resulted in a $10 \pm 5\%$ decrease in the stiffest direction of linear compressibility along the *c*-axis, leading to stronger elastic anisotropy compared with the Fe-free CF phase. The NaO₈ polyhedra volume is 2.6 times larger and about 60% more compressible than the octahedral (Al,Si)O₆ sites, with $K_{\text{NaO}_8} = 127 \text{ GPa}$ and $K_{(\text{Al,Si})\text{O}_6} \sim 304 \text{ GPa}$. Raman spectra of the pure CF-type NaAlSiO₄ sample shows that the pressure coefficient of the mean vibrational mode, $1.60(7) \text{ cm}^{-1}/\text{GPa}$, is slightly higher than $1.36(6) \text{ cm}^{-1}/\text{GPa}$ obtained for the Fe-bearing CF-NaAlSiO₄ sample. The ability of CF-type phases to contain incompatible elements such as Na beyond the stability field of jadeite requires larger and less-compressible NaO₈ polyhedra. Detailed high-pressure crystallographic information for the CF phases provides knowledge on how large alkali metals are hosted in alumina framework structures with stability well into the lowermost mantle.

Keywords: CF-type NaAlSiO₄, single-crystal structure refinements, incompatible Na elements, high pressures, Raman spectroscopy, lower mantle

INTRODUCTION

The bulk lower mantle is considered well mixed above the D'' layer, yet regional heterogeneities are identified by seismology and geochemical studies (e.g., Jenkins et al. 2017; Romanowicz and Wenk 2017). Calcium-ferrite (CF) type phases and the new hexagonal aluminous phase (NAL phase) may collectively account for 10–30 vol% of subducted oceanic crust below ~2700 km and therefore likely play an important role in the observed regional-scale seismological and geochemical heterogeneities (Bina and Helffrich 2014; French and Romanowicz 2014; Fukao and Obayashi 2013; Litasov and Ohtani 2005; Wu et al. 2016, 2017). However, the high-pressure behaviors (e.g., structure, stability, and elasticity) of the alkali-rich aluminous high-pressure phases remain poorly known compared with other lower mantle minerals such as bridgmanite [(Mg,Fe)SiO₃], davemaoite (CaSiO₃), and ferropericlase [(Mg,Fe)O] (Fujino et al. 2012; Ono et al. 2004; Wentzcovitch et al. 1995). Determining the structure and thermo-

dynamic properties of the major alkali-rich phases will therefore improve computational models of slab dynamics as well as our understanding of the behavior of incompatible elements in the lowermost mantle.

Average mid-ocean ridge basalt contains 10–12 wt% CaO and 2–3 wt% Na₂O, largely in plagioclase and clinopyroxenes in the upper mantle (Sun et al. 1979). On subduction to below 50–60 km, the basalt-eclogite transition changes the mineralogy of MORB where Ca-pyroxene (diopside), Na-pyroxene (jadeite) and garnet host the majority of alkali metals and aluminum (Yoder and Tilley 1962; Ringwood and Green 1966). Below ~300 km, pyroxene and garnet form a solution of majoritic garnet but below the transition zone (410–660 km) the breakdown of majoritic garnet leads to bridgmanite, davemaoite, and stishovite, where Al, the majority of Na, and some Ca are hosted in the CF-type and/or NAL-phases (depending on depth) with complex chemical compositions (Kesson et al. 1994; Ono et al. 2001; Ricolleau et al. 2010).

CF phases crystallizing in the orthorhombic system (space group *Pbnm*) display solid solutions with the general formula A₃B₆O₁₂, where A represents a large mono- or divalent cations, like Na⁺, K⁺, or Ca²⁺, and B is a sixfold-coordinated cation site

* E-mail: fei.qin@cugb.edu.cn. Orcid 0000-0001-9540-278X

† Orcid 0000-0001-8978-3483

‡ Orcid 0000-0002-6679-892X

§ Orcid 0000-0002-9746-958X

occupied by Mg²⁺ and mixed-valence Fe. Incorporation of Al³⁺ or Si⁴⁺ into the octahedral site leads to CF-type phases CaAl₂O₄, MgAl₂O₄, and NaAlSiO₄ (Irifune et al. 1991; Liu 1977; Reid and Ringwood 1969). Along the NaAlSiO₄-MgAl₂O₄ join, NAL is formed as a single phase up to 34 GPa, whereas above 45 GPa, NaAlSiO₄ and MgAl₂O₄ coexist as separate phases in the calcium-ferrite structure (Imada et al. 2011). Given that these likely exist as separate phases over most of the depth range in lower mantle, experimental determination of their physical properties is needed to properly estimate the density and velocity of subducted slabs (Ricolleau et al. 2010). Furthermore, by examining the influence of iron incorporation it is also possible to evaluate potential impacts of iron spin-pairing transitions (e.g., Lobanov et al. 2017; Wu et al. 2017).

To gain insight into the elasticity and equations of state as well as alkali storage mechanisms, we have undertaken high-precision, single-crystal structure determinations of Fe-free and Fe-bearing CF phases up to ~45 GPa in situ using synchrotron-based single-crystal X-ray diffraction. Vibrational properties of these structures were determined by Raman spectroscopy. These results provide comprehensive understanding of the crystallographic information of such alkali-bearing CF phases under lower mantle conditions, thus improving our knowledge of proper chemical and physical properties of these important lower mantle alkali-dominated phases, and shedding new light on alkali reservoirs in the Earth's deep mantle.

MATERIALS AND METHODS

Samples for the current study were synthesized in experimental runs #5K2124 (Fe-free) and #5K2681 (Fe-bearing) at 25 GPa and 1600 °C using a 5000-ton Kawai-type multi-anvil pressure apparatus (USSA-5000) at the Institute for Study of the Earth's Interior (ISEI), Okayama University at Misasa, Japan. Details of the sample synthesis and compositional characterization are reported in Wu et al. (2017). Briefly, a stoichiometric mixture of high-purity Na₂CO₃, Al₂O₃, and SiO₂ were mixed with a molar ratio of 1:1:2 and used as the starting material. For the Fe-bearing sample, iron was added as ⁵⁷Fe₂O₃ with >95% enrichment in ⁵⁷Fe. The chemical compositions of the Fe-free and Fe-bearing samples were obtained by electron microprobe analysis as given by Wu et al. (2017) and found to be Na_{0.93}Al_{1.02}Si_{1.00}O₄ and Na_{0.88}Al_{0.99}Fe_{0.13}Si_{0.94}O₄. Their crystal structure was characterized by X-ray diffraction at GSECARS of the Advanced Photon Source (APS), Argonne National Laboratory (ANL), beamline 13-BM-C. The results confirm that both CF samples possess space group *Pbnm*, and their lattice constants are *a* = 10.166(1) Å, *b* = 8.675(9) Å, *c* = 2.7380(6) Å, and *V* = 241.5(1) Å³ for the Fe-free CF phase, and *a* = 10.189(2) Å, *b* = 8.686(7) Å, *c* = 2.7571(4) Å, and *V* = 244.0(2) Å³ for the Fe-bearing sample. Mössbauer spectroscopy shows that 90% of the iron is ferric (Fe³⁺) (Wu et al. 2017). Crystals of the CF phases measuring ~1.5 mm in maximum dimension were crushed into 30 × 40 μm chips under an optical microscope and then polished to ~10 μm thickness for the high-pressure study.

High-pressure, single-crystal X-ray diffraction experiments were carried out at GSECARS (Sector 13) of the APS, ANL, beamline 13-BM-C. A monochromatic X-ray beam with a wavelength of 0.434 Å was focused to a 15 × 15 μm² spot for the diamond-anvil cell experiment (Zhang et al. 2017). We used a short symmetric-type diamond-anvil cells, fitted with Boehler-Almax diamond anvils with 300 μm flat culets and set into seats with 76-degree opening. A Re gasket was pre-indentated to ~40 μm thickness before laser drilling a sample chamber of ~160 μm diameter. Polished Fe-free and Fe-bearing CF samples were loaded with neon pressure medium into their respective sample chambers along with Pt foil for pressure calibration (Fei et al. 2007).

To obtain sufficiently precise constraints on the unit-cell evolution, we obtained diffraction data with multiple detector positions and for the full structure determinations at least 600 reflections were used (Online Materials¹ Fig. S1). The single-crystal structure refinements of the CF samples were carried out using ATREX/RVS, SHELXL, Olex2, and VESTA software packages (Dera et al. 2013; Dolomanov et al. 2009; Momma and Izumi 2008). A crystal structure model of Yamada et al. (1983) was used to initialize the refinement. We used isotropic atomic displacement

parameters (*U*_{iso}) for all atoms. Figures of merits of the refinements, atomic coordinates and displacement parameters of Fe-free CF phase are presented in Online Materials¹ Tables S1 and S2.

High-pressure Raman spectroscopy for the iron-bearing and pure CF-NaAlSiO₄ phases was performed up to 44.6 GPa at room temperature using Princeton-style diamond-cells with 300 μm ultralow fluorescent diamond anvils. The diamond cells for Raman spectroscopy were gas loaded with neon at HPSTAR and ruby was used as the pressure calibration (Mao et al. 1986). The pressure was determined by multiple measurements before and after each experimental run. Raman spectra were collected on a Renishaw inVia reflex Raman spectrometer with 532 nm diode-pumped solid-state laser, at Peking University. The spectrograph was calibrated using a silicon wafer, and the spectra were collected in unpolarized, backscatter geometry using a charge-coupled device detector with a resolution of 1 cm⁻¹. Each Raman spectrum was collected with an averaged exposure time of 30 s over 5 accumulations. The deconvolution of Raman spectra and peak positions were fitted using the software package PeakFit (Systat Software, Inc.)

RESULTS AND DISCUSSION

Stability and compressibility of Fe-free and Fe-bearing CF phase

Throughout the investigated pressure range (up to 41.3 and 44 GPa for Fe-free and Fe-bearing CF, respectively), no indicators of phase transformation were identified. The crystal structure of Fe-free CF-NaAlSiO₄ at 41.3 GPa is shown in Figure 1. The CF phase consists of an alumina framework composed of double chains of linked (Al,Si)₂O₆⁻ and (Al,Si)₂O₆-octahedra, while relatively large alkali Na sites are located in the eight-fold coordination sites in tunnels formed by the octahedral chains, hereafter denoted NaO₈-polyhedra. The quality of diffraction patterns used to carry out structure refinements at low (~2 GPa) and high (~40 GPa) pressures are illustrated by the CCD images shown in Online Materials¹ Figure S1.

Lattice parameters of the CF phase are consistently refined to an orthorhombic cell (*Pbnm* and *Z* = 4) (Fig. 2). Volume compression and axial compression data of both CF phases at different pressures are given in Online Materials¹ Tables S3 and S4. Pressure-volume data were fitted to a third-order Birch-Murnaghan equation of state (EoS) using error-weighted least squares with EoSFit7c software (Angel et al. 2014). Under ambient conditions, the measured *V*₀ values are 241.5(1) and 244.0(2) Å³ for the Fe-free

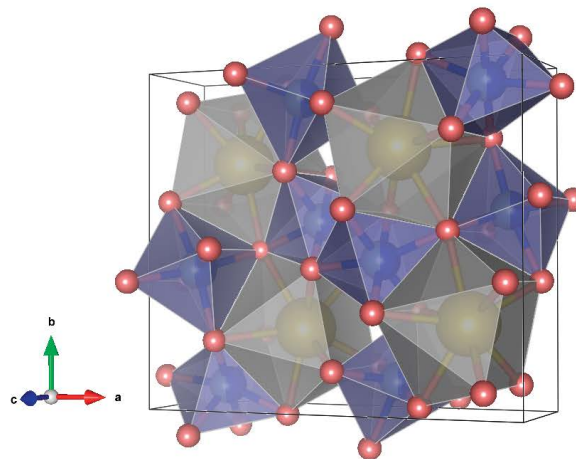


FIGURE 1. The crystal structure of the CF phase, determined at 41.3 GPa. The gray polyhedra corresponded to the A sites, occupied by Na⁺ or Fe²⁺, and the smaller purple octahedra correspond to the B sites, occupied by Al³⁺ and Si⁴⁺. (Color online.)

and Fe-bearing CF sample, respectively. The best-fit, third-order Birch-Murnaghan EoS parameters yield $V_0 = 241.6(1) \text{ \AA}^3$, $K_{70} = 220(4) \text{ GPa}$, and $K'_{70} = 2.6(3)$ for Fe-free CF, and $V_0 = 244.2(2) \text{ \AA}^3$, $K_{70} = 211(6) \text{ GPa}$ with $K'_{70} = 2.6(3)$ for Fe-bearing CF. Note that at room pressure, the measured unit-cell volume and the fitted zero-pressure volume in our BM3 procedure are identical within error for both Fe-free and Fe-bearing phases. Although both CF phases exhibit broadly similar equation of state parameters, the unit-cell volume of the Fe-bearing sample is about 1% larger and about 4% more compressible than the Fe-free sample.

We also determined the axial compressibility of the lattice parameters using the linearized third-order Birch-Murnaghan EoS (Fig. 2). Details are described in Online Materials¹ Text S1. Our fitted linear moduli to a , b , and c axes are 158(5), 180(8), and 338(9) GPa for Fe-free CF phase, and 158(11), 181(7), and 306(16) GPa for Fe-bearing CF sample, respectively, which indicate a - and b -axes exhibit similar linear moduli for both CF phases. The addition of Fe into the CF phase leads to a decrease in the linear compressibility of the c -axis compared with Fe-free phase. The relative axial compressibility scheme is $\beta_a > \beta_b > \beta_c$ for both phases. Ratios of zero-pressure axial compressibility between the three axes are 2.14:1.88:1 for Fe-free and 1.94:1.69:1 for Fe-bearing sample, which suggests strong elastic anisotropy on compression, with the c -axis being the stiffest direction within the structure.

The room temperature equations of state for CF phases determined in this study are shown in Figure 3, with volume normalized to measured V_0 in order to aid in comparison with previous studies. The absolute difference between our equation of state parameters and those from previous work (Online Materials¹ Table S5) depends on many factors including (among others) data precision, data density, crystal quality, and the experimental pressure range, resulting in the usual trade-offs between V_0 , K_{70} , and K'_{70} fitted to different data sets, and complicating a quantitative assessment of the effect of Fe substitution on the compressibility of CF phase.

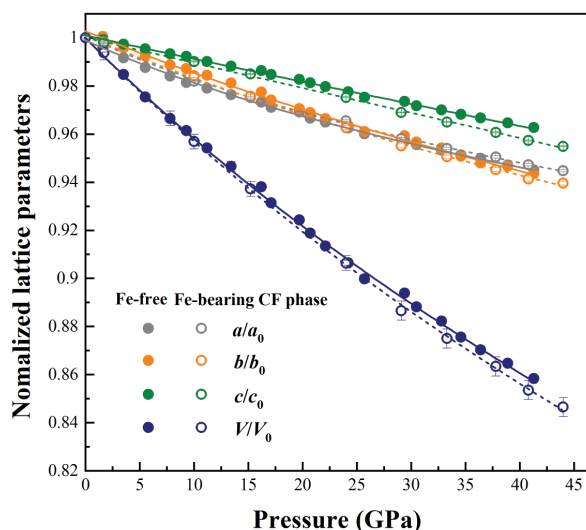


FIGURE 2. Normalized lattice parameters of Fe-free (filled circles) and Fe-bearing (open circles) CF phases as a function of pressure at room temperature. Equations of state fits are shown by solid lines for the Fe-free phase and dashed lines for the Fe-bearing CF phase. (Color online.)

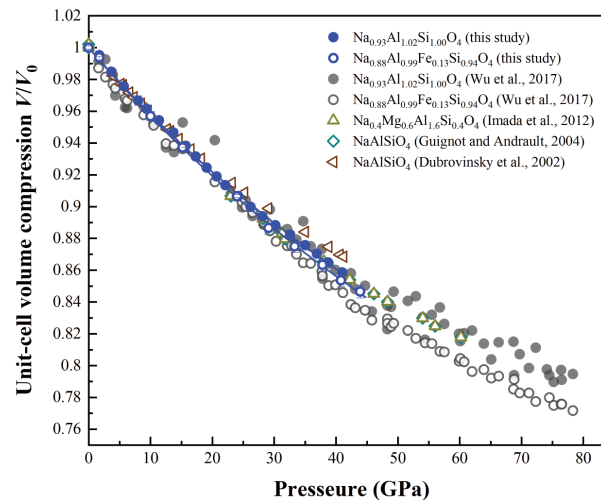


FIGURE 3. Pressure-volume data for the CF-phase (filled circles) and Fe-bearing CF phase (open circles) from this study compared with other compositions from previous work (Guignot and Andraut 2004; Imada et al. 2012; Wu et al. 2017). Solid curves show the fitted BM3 equations of state from this study. (Color online.)

By measuring both pure-CF and Fe-bearing CF phases in the same study with high-quality single crystals, we were able to tightly constrain the values of K_{70} and K'_{70} for both crystals under similar experimental parameters, finding that $\text{Fe}_{\text{tot}} = 0.13 \text{ pfu}$ in the CF phase leads to $3.2 \pm 1.9\%$ reduction in the bulk modulus compared with the Fe-free sample. The lower bulk moduli values of $K_{70} = 201(9) \text{ GPa}$ reported for the CF-phase by Wu et al. (2017), who also determined high-spin [$K_{70} = 208(3) \text{ GPa}$] and low-spin [$K_{70} = 202(7) \text{ GPa}$] bulk moduli for Fe-bearing CF phase were fitted with relatively high values of K'_{70} (fixed at 4), which are, however, poorly constrained. The derived EoS parameters obtained in this study are statistically higher than that obtained by Guignot and Andraut (2004) with $K_{70} = 185(5) \text{ GPa}$ but in good agreement with previously reported values of $K_{70} = 214(14) \text{ GPa}$, $K'_{70} = 3.6(5)$ (Imada et al. 2012) and $K_{70} = 220(1) \text{ GPa}$, $K'_{70} = 4.1(1)$ (Dubrovinsky et al. 2002).

Generally, CF phases in MORB compositions exhibit complex solid solutions but for simplicity can be considered along the NaAlSiO_4 - MgAl_2O_4 join (Imada et al. 2011). By comparison, solid solutions between NaAlSiO_4 and MgAl_2O_4 in the CaFe_2O_4 structure type show roughly similar density between these two end members. However, there is a very broad range of reported values for the bulk modulus of the CaFe_2O_4 -type MgAl_2O_4 phase in MORB composition, ranging from 184–243 GPa (Funamori et al. 1998; Irifune et al. 2002; Guignot and Andraut 2004; Ono et al. 2005). The thermal equation of state of MgAl_2O_4 has also been investigated using multi-anvil apparatus and DAC techniques by Sueda et al. (2009), who reported 205(6) GPa for the room-temperature bulk modulus.

High-pressure structure evolution of CF phase

To better understand the compression mechanisms of CF-type NaAlSiO_4 , we analyzed the structure and evolution of the polyhedral elements on compression at selected pressures. Here we used two parameters to characterize the compression of each

polyhedron: the polyhedral volume and the mean bond length. Results are given in Online Materials¹ Table S6. More details on the high-pressure structure refinements of the Fe-free sample will be discussed next.

The bond lengths of Na-O, (Al,Si)1-O, and (Al,Si)2-O as a function of pressure are shown in Figure 4. Average (Al,Si)-O distances related to the (Al,Si)1 and (Al,Si)2 sites are 1.856 and 1.876 Å at room pressure, respectively. By comparing with those aluminous high-pressure phases, these values are in good agreement with 1.929 Å in NaAlSi₂O₆ jadeite (Cameron et al. 1973) and 1.887 Å in Mg₃Al₂Si₃O₁₂ pyrope (Novak and Gibbs 1971), which are typical values for the six-coordinated Al-O distances. During static compression, all of the bond distances decrease linearly in the range of 0.00168–0.00172 Å/GPa for (Al,Si)-O bond, while the shortening of Na-O bonds are about twice than that of the (Al,Si)-site octahedral bonds. Over the whole pressure range of this study, the mean bond length of Na-O is shortened by 6.7%, whereas the (Al,Si)-O bonds are shortened by only 3.6% for (Al,Si)1-O and 3.7% for (Al,Si)2-O.

The structural evolution of all the coordination polyhedra is presented in Figure 5. The average (Al,Si)O₆ volume is 8.48(2) Å³ at ambient pressure and decreases to 7.62(2) Å³ at 41.0 GPa, while the volume of NaO₈-polyhedron is about 2.6 times larger, and decreases from 22.40(3) to 18.37(2) Å³ between 0 and 41.0 GPa. The average (Al,Si)O₆ volume has a much smaller value and is significantly more incompressible than the NaO₈-polyhedron. In particular, the (Al,Si)O₆ octahedron is much stiffer with an average bulk modulus of ~304 GPa compared with the $K_0^{\text{NaO}_8}$ of 127 GPa within the whole pressure range, when both K'_0 fixed at 4. Our value of $K_0^{\text{SiO}_6}$ for CF phase is in excellent agreement with the compressibility of SiO₆ octahedron in stishovite SiO₂ ($K_0^{\text{SiO}_6}$ = 303–346 GPa), another important phase in the lower mantle (Andrault et al. 1998).

The distortion index (D) describes the polyhedral distortion, defined as

$$D = \frac{1}{n} \sum_{i=1}^n \frac{|l_i - l_{\text{ave}}|}{l_{\text{ave}}}$$

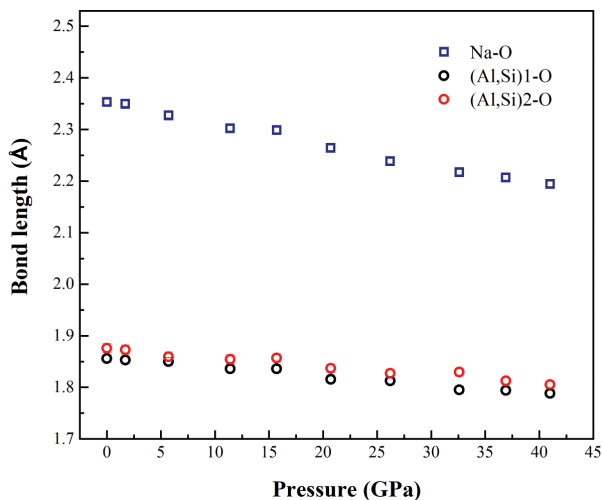


FIGURE 4. Pressure dependence of the mean bond lengths of the two distinct (Al,Si)O₆ octahedra and the NaO₈ polyhedra in the pure CF phase. (Color online.)

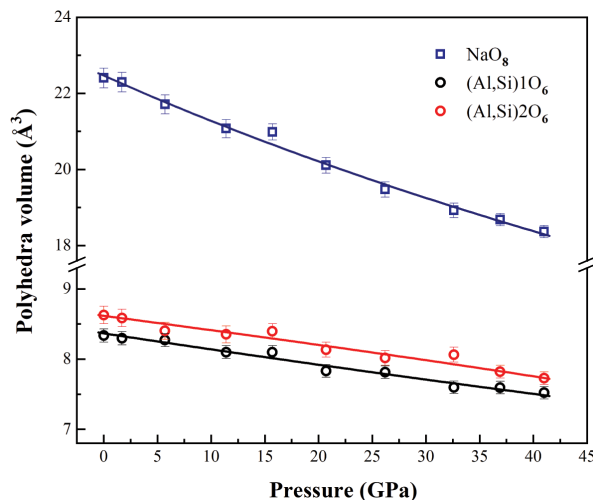


FIGURE 5. Pressure dependence of the polyhedral volumes for the pure CF phase. (Color online.)

where l_i is the distance from the central cation to the i_{th} surrounding oxygen and l_{ave} is the average distance (Baur 1974; Momma and Izumi 2008). In this study, we found that NaO₈ polyhedra have higher distortion indices than the (Al,Si)O₆ octahedra across the experimental pressure range. At 41 GPa, D_{NaO_8} is 0.029 while the average $D_{(\text{Al,Si})\text{O}_6}$ is 0.0078. Distortion index values of the NaO₈ did not change beyond error during compression, indicating that the NaO₈ polyhedra have less structural deformation compared with the (Al,Si)O₆ upon compression (Fig. 6).

Vibrational modes and Grüneisen parameters

In situ Raman spectroscopy was conducted up to 44.6 GPa on both Fe-free and Fe-bearing crystals taken from the same synthesis runs used in the XRD study. Selected spectra of both crystals with increasing pressure are presented in Figure 7. As the Raman active modes are $18A_g + 9B_{1g} + 18B_{2g} + 9B_{3g}$, a total of 54 Raman active vibrations modes are expected. Unfortunately, the data quality is not high enough to deconvolute and assign all the peaks. The smaller number of observed modes is due to weak intensity, peak overlap, and orientation dependence. In this study, around 14 Raman peaks were observed for the CF in the Raman shift range of 120–150 cm⁻¹. Peak positions of the major observed modes as a function of pressure are provided in Figure 7 and Online Materials¹ Table S7. All observed Raman peaks shift to higher frequency with increasing pressure, and some broad bands may consist of several Raman active modes having very close frequencies.

There have been numerous investigations on MgAl₂O₄, CaAl₂O₄, and their solid solutions with Raman spectroscopy (Kojitani et al. 2013; Ono et al. 2009). Yet, there is no detailed Raman spectroscopic study on Fe-free and Fe-bearing CF phase. As shown in Figure 7, Raman modes located between 680–900 cm⁻¹ become stronger and sharper at higher pressures in both phases. At ambient conditions, the peak at 190 cm⁻¹ of Fe-free CF phase can be attributed to the vibrations of the Na⁺ ions, while this peak is not observed in the Fe-bearing sample (Fei et al. 2020; Kojitani et al. 2013). The vibrational modes at ~348 and 331 cm⁻¹ in Fe-free and Fe-bearing CF phase, respectively, can be assigned to A_g modes

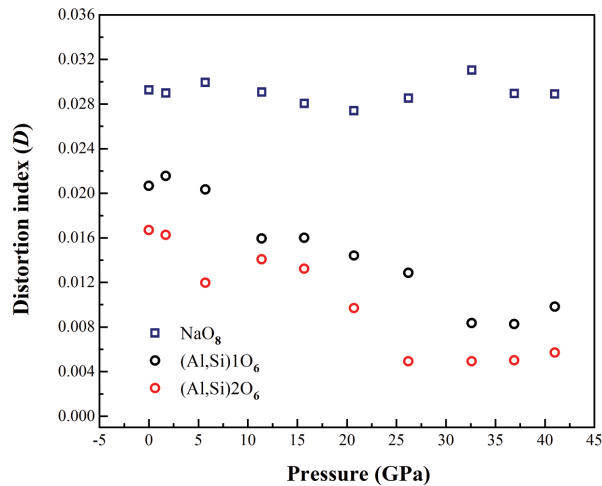


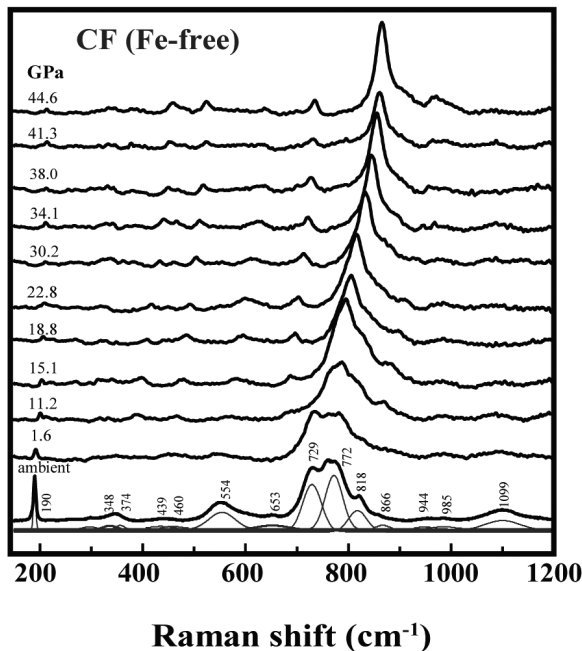
FIGURE 6. Pressure dependence of the distortion indices of the two distinct (Al,Si)O₆ octahedra and NaO₈ polyhedra for the pure CF phase. (Color online.)

with translation of Al³⁺ (Kojitani et al. 2013). Mode frequencies at 374, 439, 460, 554, and 653 cm⁻¹ in the Fe-free sample and at 386, 453, 474, 535, and 631 cm⁻¹ of Fe-bearing sample can be attributed to the O-Si-O and Si-O-Si (or Al) bending, which are accordance with the MgAl₂O₄ and CaAl₂O₄ in CF structure (Kojitani et al. 2013). In the frequency range of 680–900 cm⁻¹, the most intense peaks at 729, 772 cm⁻¹ (Fe-free CF) and 720, 799 cm⁻¹ (Fe-bearing CF) are mainly caused by the vibrational modes related to the octahedral sites. It should be noted that peak broadenings in the frequency range of 400–660 and 680–900 cm⁻¹

are generally associated with structural disorder over lattice sites, i.e., Si, Al, and Fe disorder over the octahedral site in the CF structure (Kojitani et al. 2013). Therefore, spectral deconvolution in the region between 680–900 cm⁻¹ produces three main peaks around 720, 799, 839 cm⁻¹ and 729, 772, 818 cm⁻¹ assigned to the (Al/Si)O₆ octahedral sites in Fe-rich and Fe-free CF phase, respectively (Online Materials¹ Fig. S3). It was found that the bands appearing at the 680–900 cm⁻¹ region in Fe-bearing CF phase tend to be broader than the pure-CF, due to presence of Fe³⁺ in the octahedral sites. On this basis, the Raman bands become far apart with elevated pressure, indicating less disorder in the octahedral Fe environments (Online Materials¹ Fig. S3). Additionally, at higher frequencies, the appearance of the peaks at 944, 985, 1099 cm⁻¹ and 908, 980, 1080 cm⁻¹ in Fe-free and Fe-rich CF sample, respectively, are probably caused by Si-O_{nb} (non-bridged oxygen), Si-O_{br} (bridged oxygen) bending asymmetric and symmetric stretchings (Prencipe 2012).

Mode Grüneisen parameters (γ_i) were calculated using $\gamma_i = (K_0/v_i)(d\nu_i/dP)_T$, where ν_i is the wavenumber of the i^{th} mode and K_0 is the bulk modulus at room temperature (Online Materials¹ Table S7). Here, we used the isothermal bulk modulus K_0 of 220(4) and 211(6) GPa for Fe-free and Fe-bearing CF phase, respectively, which were obtained by the BM3 fit. The resulting mean pressure coefficient of the whole structure for pure CF-NaAlSiO₄ of 1.61(7) cm⁻¹/GPa is slightly higher than 1.40(6) cm⁻¹/GPa found for Fe-bearing sample. Correspondingly, the calculated mode Grüneisen parameters determined in this study range from 0.31(2)–0.94(2) for the pure-CF, and 0.25(3)–0.84(2) for the Fe-bearing CF phase, with average values from all the observed modes of 0.58(1) and 0.54(2), respectively. As for the octahedral site vibrations in both phases, the calculated γ values fall gener-

(A)



(B)

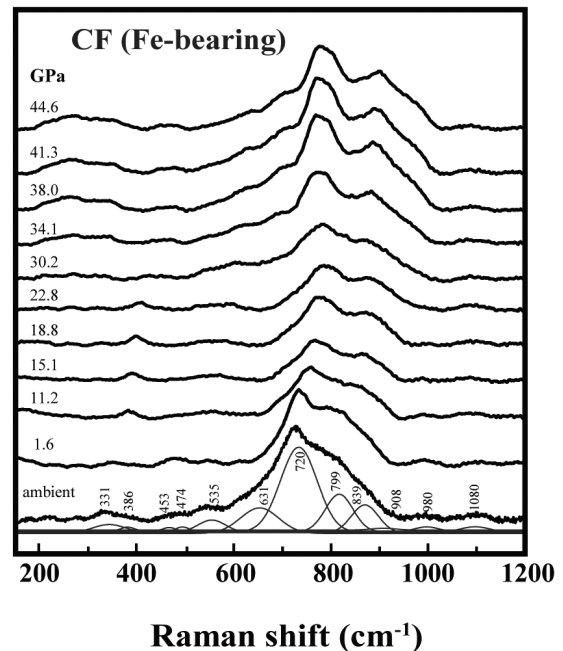


FIGURE 7. Selected Raman spectra of Fe-free CF phase (a) and Fe-bearing CF phase (b) at various pressures. Individual plots of deconvoluted Raman spectra at ambient conditions are also shown.

ally in the range of 0.57–0.84, which are comparable with those experimental determined modes with AlO₆ octahedra for MgAl₂O₄ in the CF-type structure (Kojitani et al. 2013). The mean pressure coefficient of octahedral site-derived mode in Fe-bearing CF phase of 2.78(7) cm⁻¹/GPa is larger than 2.17(6) cm⁻¹/GPa found in Fe-free sample, consistent with the higher compressibility of the Fe-bearing phase relative to Fe-free CF phase. We therefore conclude that the major difference in compressibility between the two structures is related to the Al/Fe-O bonds in octahedral sites in particular along the *c*-axis.

IMPLICATIONS

Generally, the structural compression mechanisms of the CF and NAL phases can be compared with the structural shrinkage in K-hollandite. With increasing pressure, a distortion of the (Al,Si)O₆ octahedral framework, which forms the tunnel structure, contracts and leads to more compact tunnels. Since the VIII-K-O bond in K-hollandite is one of the most compressible bonds among the metal-oxygen pairs in oxide minerals, KO₈ polyhedra are very compressible and can be compared to the bulk modulus of NaO₈ in the CF phase (Mookherjee and Steinle-Neumann 2009; Zhang et al. 1993). Furthermore, in comparison to jadeite-NaAlSi₂O₆ (McCarthy et al. 2008; Posner et al. 2014), the longer Na-O bonds and low degree of NaO₈ polyhedra distortion in the CF phase determined here at high pressures likely contribute to its wide stability over lower mantle conditions.

Na-bearing majorite and Na-rich pyroxene (e.g., NaAlSi₂O₆ jadeite, NaFe³⁺Si₂O₆ aegirine) have similar chemical compositions and have also considered as potential hosts for Na in the Earth's mantle (Bindi et al. 2011; Xu et al. 2017). Previous studies have indicated that aegirine remains in the monoclinic *C2/c* structure up to 60 GPa, with the NaO₈ polyhedron likely controlling bulk compressibility (Xu et al. 2017). However, the incorporation of Fe³⁺ to Na-pyroxene significantly increases the bulk modulus as well as the transition pressure for the pyroxene to garnet transition (Xu et al. 2017; Matrosova et al. 2019). Although sodium is significantly enriched in continental crust compared with oceanic crust, Na is an important incompatible element in the mantle because it partitions strongly into the MORB-forming melts below the spreading ridges (Hofmann 1988). Thus, subduction of MORB recycles Na into the mantle where it contributes to melting in the upper-mantle wedge but is also likely carried deeper into the mantle. The CF phase is regarded as the only Na-dominated stable phase in the lower mantle down to ~2700 km.

Considering the potentially significant volume proportion of CF and NAL phases in deeply subducted MORB, the elastic properties of these minerals and their compositional solid solutions are important for estimates of density and velocity of MORB. In more recent studies, coupled substitutions of Al³⁺ and Mg²⁺ in the CF structure by Na⁺ and Si⁴⁺ has limited influence on its elastic constants, but slightly weaken the elastic wave anisotropy (Zhao et al. 2018; Wang et al. 2020). Further investigations of the crystal chemistry on the CF phase at the pressure and temperature relevant to the lower mantle conditions are necessary. Most importantly, adopting the thermo-elastic parameters of the CF-structure end-member to estimate the thermo-elastic properties of complex aluminous solid solutions would improve our understanding of the role that recycled oceanic crust plays in the

global alkali cycle with implications for the long-term evolution and internal heating of the Earth's mantle.

FUNDING

This research was supported by the National Natural Science Foundation of China (grant no. 42202040 and 42172076), the SinoProbe laboratory of Chinese Academy of Geological Sciences (grant no. 202208), and the Fundamental Research Funds for the Central Universities (grant no. 590421013). S.D.J. acknowledges support from the U.S. National Science Foundation Grant EAR-1853521. Work performed at GSECARS (Sector 13) of the Advanced Photon Source (APS) is supported by the NSF EAR-1634415 and the Department of Energy (DOE) DE-FG02-94ER1446. The APS at Argonne National Laboratory is supported by the DOE, Office of Science, under Contract No. DE-AC02-06CH11357. Experiments at Sector 13-BM-C of the APS used the PX² facility, supported by GSECARS and COMPRES under NSF Cooperative Agreement EAR-1661511. Use of the COMPRES-GSECARS gas loading system was supported by COMPRES under NSF Cooperative Agreement EAR-1606856.

REFERENCES CITED

- Andraut, D., Fiquet, G., Guyot, F., and Hanfland, M. (1998) Pressure-induced landau-type transition in stishovite. *Science*, 282, 720–724, <https://doi.org/10.1126/science.282.5389.720>.
- Angel, R.J., Alvaro, M., and Gonzalez-Platas, J. (2014) EosFit7c and a Fortran module (library) for equation of state calculations. *Zeitschrift für Kristallographie: Crystal-line Materials*, 229, 405–419, <https://doi.org/10.1515/zkri-2013-1711>.
- Baur, W.H. (1974) The geometry of polyhedral distortions. Predictive relationships for the phosphate group. *Acta Crystallographica*, B30, 1195–1215, <https://doi.org/10.1107/S0567740874004560>.
- Bina, C. and Helffrich, G. (2014) Geophysical constraints on mantle composition. In H.D. Holland and K.K. Turekian, Eds., *Treatise on Geochemistry*, p. 41–65. Elsevier.
- Bindi, L., Dymshits, A.M., Bobrov, A.V., Litasov, K.D., Shatskiy, A.F., Ohtani, E., and Litvin, Y.A. (2011) Crystal chemistry of sodium in the Earth's interior: The structure of Na₂MgSi₂O₁₂ synthesized at 17.5 GPa and 1700 °C. *American Mineralogist*, 96, 447–450, <https://doi.org/10.2138/am.2011.3716>.
- Cameron, M., Sueno, S., Prewitt, C.T., and Papike, J.J. (1973) High-temperature crystal chemistry of acmite, diopside, hedenbergite jadeite, spodumene and ureyite. *American Mineralogist*, 58, 594–618.
- Dera, P., Zhuravlev, K., Prakapenka, V.B., Rivers, M.L., Finkelstein, G.J., Grubor-Urošević, O., Tschauner, O., Clark, S.M., and Downs, R.T. (2013) High pressure single-crystal micro X-ray diffraction analysis with GSE_ADA/RSV software. *High Pressure Research*, 33, 466–484, <https://doi.org/10.1080/08957959.2013.806504>.
- Dolomanov, O.V., Bourhis, L.J., Gildea, R.J., Howard, J.A., and Puschmann, H. (2009) OLEX2: A complete structure solution, refinement and analysis program. *Journal of Applied Crystallography*, 42, 339–341, <https://doi.org/10.1107/S0021889808042726>.
- Dubrovinsky, L.S., Dubrovinskaia, N.A., Prokopenko, V.B., and Le Bihan, T. (2002) Equation of state and crystal structure of NaAlSiO₄ with calcium-ferrite type structure in the conditions of the lower mantle. *High Pressure Research*, 22, 495–499, <https://doi.org/10.1080/08957950212807>.
- Fei, Y., Ricolleau, A., Frank, M., Mibe, K., Shen, G., and Prakapenka, V. (2007) Toward an internally consistent pressure scale. *Proceedings of the National Academy of Sciences*, 104, 9182–9186, <https://doi.org/10.1073/pnas.0609013104>.
- Fei, G., Song, J., Chen, X., and Liu, X. (2020) Discovery of pressure-induced monoclinic to monoclinic phase transition above 60 GPa in single crystal NaAlSi₂O₆ jadeite. *Journal of Raman Spectroscopy*, 51, 844–850, <https://doi.org/10.1002/jrs.5837>.
- French, S.W. and Romanowicz, B.A. (2014) Whole-mantle radially anisotropic shear velocity structure from spectral-element waveform tomography. *Geophysical Journal International*, 199, 1303–1327, <https://doi.org/10.1093/gji/ggu334>.
- Fujino, K., Nishio-Hamane, D., Seto, Y., Sata, N., Nagai, T., Shinmei, T., Irfune, T., Ishii, H., Hiraoka, N., Cai, Y.Q., and others. (2012) Spin transition of ferric iron in Al-bearing Mg-perovskite up to 200 GPa and its implication for the lower mantle. *Earth and Planetary Science Letters*, 317–318, 407–412, <https://doi.org/10.1016/j.epsl.2011.12.006>.
- Fukao, Y. and Obayashi, M. (2013) Subducted slabs stagnant above, penetrating through, and trapped below the 660 km discontinuity. *Journal of Geophysical Research Solid Earth*, 118, 5920–5938, <https://doi.org/10.1002/2013JB010466>.
- Funamori, N., Jeanloz, R., Nguyen, J.H., Kavner, A., Caldwell, W.A., Fujino, K., Miyajima, N., Shinmei, T., and Tomioka, N. (1998) High-pressure transformation in MgAl₂O₄. *Journal of Geophysical Research*, 103 (B9), 20813–20818, <https://doi.org/10.1029/98JB01575>.
- Guignot, N. and Andraut, D. (2004) Equations of state of Na-K-Al host phases and implications for MORB density in the lower mantle. *Physics of the Earth and Planetary Interiors*, 143–144, 107–128, <https://doi.org/10.1016/j.pepi.2003.09.014>.
- Hofmann, A.W. (1988) Chemical differentiation of the Earth: The relationship between mantle, continental crust, and oceanic crust. *Earth and Planetary Science Letters*, 90, 297–314, [https://doi.org/10.1016/0012-821X\(88\)90132-X](https://doi.org/10.1016/0012-821X(88)90132-X).

- Imada, S., Hirose, K., and Ohishi, Y. (2011) Stabilities of NAL and Ca-ferrite-type phases on the join NaAlSi₃O₈-MgAl₂O₄ at high pressure. *Physics and Chemistry of Minerals*, 38, 557–560, <https://doi.org/10.1007/s00269-011-0427-2>.
- Imada, S., Hirose, K., Komabayashi, T., Suzuki, T., and Ohishi, Y. (2012) Compression of Na_{0.6}Mg_{0.6}Al_{1.6}Si_{0.4}O₄ NAL and Ca-ferrite-type phases. *Physics and Chemistry of Minerals*, 39, 525–530, <https://doi.org/10.1007/s00269-012-0508-x>.
- Irifune, T., Fujino, K., and Ohtani, E. (1991) A new high-pressure form of MgAl₂O₄. *Nature*, 349, 409–411, <https://doi.org/10.1038/349409a0>.
- Irifune, T., Naka, H., Sanehira, T., Inoue, T., and Funakoshi, K. (2002) In situ X-ray observations of phase transitions in MgAl₂O₄ spinel to 40 GPa using multianvil apparatus with sintered diamond anvils. *Physics and Chemistry of Minerals*, 29, 645–654, <https://doi.org/10.1007/s00269-002-0275-1>.
- Jenkins, J., Deuss, A., and Cottaar, S. (2017) Converted phases from sharp 1000 km depth mid-mantle heterogeneity beneath Western Europe. *Earth and Planetary Science Letters*, 459, 196–207, <https://doi.org/10.1016/j.epsl.2016.11.031>.
- Kesson, S.E., Fitz Gerald, J.D., and Shelley, J.M.G. (1994) Mineral chemistry and density of subducted basaltic crust at lower-mantle pressures. *Nature*, 372, 767–769, <https://doi.org/10.1038/372767a0>.
- Kojitani, H., Többsen, D.M., and Akaogi, M. (2013) High-pressure Raman spectroscopy, vibrational mode calculation, and heat capacity calculation of calcium ferrite-type MgAl₂O₄ and CaAl₂O₄. *American Mineralogist*, 98, 197–206, <https://doi.org/10.2138/am.2013.4095>.
- Litasov, K.D. and Ohtani, E. (2005) Phase relations in hydrous MORB at 18–28 GPa: Implications for heterogeneity of the lower mantle. *Physics of the Earth and Planetary Interiors*, 150, 239–263, <https://doi.org/10.1016/j.pepi.2004.10.010>.
- Liu, L. (1977) High pressure NaAlSi₃O₈: The first silicate calcium ferrite isotope. *Geophysical Research Letters*, 4, 183–186, <https://doi.org/10.1029/GL004i005p00183>.
- Lobanov, S.S., Hsu, H., Lin, J.F., Yoshino, T., and Goncharov, A.F. (2017) Optical signatures of low spin Fe²⁺ in NAL at high pressure. *Journal of Geophysical Research*. *Solid Earth*, 122, 3565–3573, <https://doi.org/10.1002/2017JB014134>.
- Mao, H.K., Xu, J.A., and Bell, P.M. (1986) Calibration of the ruby pressure gauge to 800 kbar under quasi-hydrostatic conditions. *Journal of Geophysical Research*, 91 (B5), 4673–4676, <https://doi.org/10.1029/JB091iB05p04673>.
- Matrosova, E.A., Ismailova, L., Bobrov, A.V., Bykova, E., Bykov, M., Glazyrin, K., Bindi, L., Ovsyannikov, S.V., Aksenov, S.M., Pushcharovsky, D.Y., and Dubrovinsky, L. (2019) Compressibility of two Na-rich clinopyroxenes: A synchrotron single-crystal X-ray diffraction study. *American Mineralogist*, 104, 905–913, <https://doi.org/10.2138/am-2019-6658>.
- McCarthy, A.C., Downs, R.T., and Thompson, R.M. (2008) Compressibility trends of the clinopyroxenes, and in-situ high-pressure single-crystal X-ray diffraction study of jadeite. *American Mineralogist*, 93, 198–209, <https://doi.org/10.2138/am.2008.2521>.
- Momma, K. and Izumi, F. (2008) VESTA: A three-dimensional visualization system for electronic and structural analysis. *Journal of Applied Crystallography*, 41, 653–658, <https://doi.org/10.1107/S0021889808012016>.
- Mookherjee, M. and Steinle-Neumann, G. (2009) Detecting deeply subducted crust from the elasticity of hollandite. *Earth and Planetary Science Letters*, 288, 349–358, <https://doi.org/10.1016/j.epsl.2009.09.037>.
- Novak, G.A. and Gibbs, G.V. (1971) The crystal chemistry of the silicate garnets. *American Mineralogist*, 56, 791–825.
- Ono, S., Ito, E., and Katsura, T. (2001) Mineralogy of subducted basaltic crust (MORB) from 25 to 37 GPa, and chemical heterogeneity of the lower mantle. *Earth and Planetary Science Letters*, 190, 57–63, [https://doi.org/10.1016/S0012-821X\(01\)00375-2](https://doi.org/10.1016/S0012-821X(01)00375-2).
- Ono, S., Ohishi, Y., and Mibe, K. (2004) Phase transition of Ca-perovskite and stability of Al-bearing Mg-perovskite in the lower mantle. *American Mineralogist*, 89, 1480–1485, <https://doi.org/10.2138/am-2004-1016>.
- Ono, S., Ohishi, Y., Isshiki, M., and Watanuki, T. (2005) In situ X-ray observations of phase assemblages in peridotite and basalt compositions at lower mantle conditions: Implications for density of subducted oceanic plate. *Journal of Geophysical Research Solid Earth*, 110 (B2), <https://doi.org/10.1029/2004JB003196>.
- Ono, A., Akaogi, M., Kojitani, H., Yamashita, K., and Kobayashi, M. (2009) High-pressure phase relations and thermodynamic properties of hexagonal aluminous phase and calcium-ferrite phase in the systems NaAlSi₃O₈-MgAl₂O₄ and CaAl₂O₄-MgAl₂O₄. *Physics of the Earth and Planetary Interiors*, 174, 39–49, <https://doi.org/10.1016/j.pepi.2008.07.028>.
- Posner, E.S., Dera, P., Downs, R.T., Lazarz, J.D., and Immen, P. (2014) High-pressure single-crystal X-ray diffraction study of jadeite and kosmochlor. *Physics and Chemistry of Minerals*, 41, 695–707, <https://doi.org/10.1007/s00269-014-0684-y>.
- Prencipe, M. (2012) Simulation of vibrational spectra of crystals by ab initio calculations: An invaluable aid in the assignment and interpretation of the Raman signals. The case of jadeite (NaAlSi₃O₈). *Journal of Raman Spectroscopy*, 43, 1567–1569, <https://doi.org/10.1002/jrs.4040>.
- Reid, A.F. and Ringwood, A.E. (1969) Newly observed high pressure transformations in Mn₂O₃, CaAl₂O₄, and ZrSiO₄. *Earth and Planetary Science Letters*, 6, 205–208, [https://doi.org/10.1016/0012-821X\(69\)90091-0](https://doi.org/10.1016/0012-821X(69)90091-0).
- Ricolleau, A., Perrillat, J.P., Fiquet, G., Daniel, I., Matas, J., Addad, A., Menguy, N., Cardon, H., Mezouar, M., and Guignot, N. (2010) Phase relations and equation of state of a natural MORB: Implications for the density profile of subducted oceanic crust in the Earth's lower mantle. *Journal of Geophysical Research Solid Earth*, 115 (B8), <https://doi.org/10.1029/2009JB006709>.
- Ringwood, A.E. and Green, D.H. (1966) An experimental investigation of the gabbroeclogite transformation and some geophysical implications. *Tectonophysics*, 3, 383–427, [https://doi.org/10.1016/0040-1951\(66\)90009-6](https://doi.org/10.1016/0040-1951(66)90009-6).
- Romanowicz, B. and Wenk, H.R. (2017) Anisotropy in the deep Earth. *Physics of the Earth and Planetary Interiors*, 269, 58–90, <https://doi.org/10.1016/j.pepi.2017.05.005>.
- Sueda, Y., Irifune, T., Sanehira, T., Yagi, T., Nishiyama, N., Kikegawa, T., and Funakoshi, K.I. (2009) Thermal equation of state of CaFe₂O₄-type MgAl₂O₄. *Physics of the Earth and Planetary Interiors*, 174, 78–85, <https://doi.org/10.1016/j.pepi.2008.07.046>.
- Sun, S.S., Nesbitt, R.W., and Sharaskin, A.Y. (1979) Geochemical characteristics of mid-ocean ridge basalts. *Earth and Planetary Science Letters*, 44, 119–138, [https://doi.org/10.1016/0012-821X\(79\)90013-X](https://doi.org/10.1016/0012-821X(79)90013-X).
- Wang, W., Xu, Y., Sun, D., Ni, S., Wentzcovitch, R., and Wu, Z. (2020) Velocity and density characteristics of subducted oceanic crust and the origin of lower-mantle heterogeneities. *Nature Communications*, 11, 1–8, <https://doi.org/10.1038/s41467-019-13720-2>.
- Wentzcovitch, R.M., Ross, N.L., and Price, G.D. (1995) Ab initio study of MgSiO₃ and CaSiO₃ perovskites at lower-mantle pressures. *Physics of the Earth and Planetary Interiors*, 90, 101–112, [https://doi.org/10.1016/0013-9201\(94\)03001-Y](https://doi.org/10.1016/0013-9201(94)03001-Y).
- Wu, Y., Wu, X., Lin, J.F., McCammon, C.A., Xiao, Y., Chow, P., and Qin, S. (2016) Spin transition of ferric iron in the NAL phase: Implications for the seismic heterogeneities of subducted slabs in the lower mantle. *Earth and Planetary Science Letters*, 434, 91–100, <https://doi.org/10.1016/j.epsl.2015.11.011>.
- Wu, Y., Qin, F., Wu, X., Huang, H.J., McCammon, C.A., Yoshino, T., Zhai, S.M., Xiao, Y.M., and Prakashenka, V.B. (2017) Spin transition of ferric iron in the calcium-ferrite type aluminous phase. *Journal of Geophysical Research: Solid Earth*, 122, 5935–5944, <https://doi.org/10.1002/2017JB014095>.
- Xu, J., Zhang, D., Fan, D., Downs, R.T., Hu, Y., and Dera, P.K. (2017) Isosymmetric pressure-induced bonding increase changes compression behavior of clinopyroxenes across jadeite-agerine solid solution in subduction zones. *Journal of Geophysical Research: Solid Earth*, 122, 142–157, <https://doi.org/10.1002/2016JB013502>.
- Yamada, H., Matsui, Y., and Ito, E. (1983) Crystal-chemical characterization of NaAlSi₃O₈ with the CaFe₂O₄ structure. *Mineralogical Magazine*, 47, 177–181, <https://doi.org/10.1180/minmag.1983.047.343.07>.
- Yoder, H.S. Jr. and Tilley, C.E. (1962) Origin of basalt magmas: An experimental study of natural and synthetic rock systems. *Journal of Petrology*, 3, 342–532, <https://doi.org/10.1093/ptrology/3.3.342>.
- Zhang, J.M., Ko, J., Hazen, R.M., and Prewitt, C.T. (1993) High-pressure crystal chemistry of KAlSi₃O₈ hollandite. *American Mineralogist*, 78, 493–499.
- Zhang, D., Dera, P.K., Eng, P.J., Stubbs, J.E., Zhang, J.S., Prakashenka, V.B., and Rivers, M.L. (2017) High pressure single crystal diffraction at PX² JoVE. *Journal of Visualized Experiments*, 119, e54660.
- Zhao, M., Zhou, H., Yin, K., Sun, Y., Liu, X., Xu, S., and Lu, X. (2018) Thermoelastic properties of aluminous phases in MORB from first-principle calculation: Implications for Earth's lower mantle. *Journal of Geophysical Research*. *Solid Earth*, 123, 10583–10596, <https://doi.org/10.1029/2018JB016491>.

MANUSCRIPT RECEIVED DECEMBER 23, 2021

MANUSCRIPT ACCEPTED JANUARY 10, 2023

ACCEPTED MANUSCRIPT ONLINE JANUARY 19, 2023

MANUSCRIPT HANDLED BY BIN CHEN

Endnote:

¹Deposit item AM-23-128432. Online Materials are free to all readers. Go online, via the table of contents or article view, and find the tab or link for supplemental materials. The CIF has been peer-reviewed by our Technical Editors.